RSC Advances

PAPER

View Article Online
View Journal | View Issue

Cite this: *RSC Adv.*, 2020, **10**, 29765

Novel light-emitting clays with structural Tb^{3+} and Eu^{3+} for chromate anion detection†

Stefano Marchesi, [a] Chiara Bisio *[ab] and Fabio Carniato *[a]

Received 30th June 2020
Accepted 5th August 2020

DOI: 10.1039/d0ra05693f

rsc.li/rsc-advances

Tb^{3+} and Eu^{3+} ions were encapsulated for the first time in the inorganic layers of a synthetic saponite clay following a one-pot synthetic approach. The co-presence of the two metal ions led to tuneable light-emitting properties, promoted by an efficient $Tb^{3+} \rightarrow Eu^{3+}$ energy transfer and enhanced Stokes shift character. To our knowledge, the so-prepared luminescent material was tested for the first time as an optical sensor for the detection of chromate anions in water.

Over the past years, synthetic smectite clays, and in particular saponite, have attracted great interest in the scientific community, due to their peculiar physico-chemical properties, such as controlled and tuneable chemical composition and specific surface area, excellent chemical versatility, high thermal stability and robustness, adjustable surface acidity and relatively simple and low cost synthesis.[1–4]

Saponite materials have been used in several applications, spanning from polymer science to heterogeneous catalysis.[5–9] Examples of their applications in the agricultural and construction fields, for environmental purposes (*i.e.* recovering of heavy metals from soils and waters) and in optical/optoelectronic devices are also reported.[10–15]

Recently, a flourishing research branch on interesting layered and porous materials (including silicas, silicates, clays, MOFs…)[16,17] has been related to their combination with rare-earth ions. Lanthanides represent key elements for many technologies used in our society (*i.e.* in energy devices, for biomedical uses…) owing to their unique electronic, magnetic, optical and catalytic properties.[18–20] Preliminary studies on the preparation of lanthanide-containing layered and/or porous materials with specific functionalities have been made, with newfound applications as sensors for targets of interests (*i.e.* biothiols, surfactants, fingerprint detection…), as luminescent thermometers,[21] or in bio-imaging fields (*i.e.* as oral MRI contrast agents).[22–30] In clay materials, for example, the lanthanides (*i.e.* Eu^{3+}, Tb^{3+}, Gd^{3+}…) were normally incorporated as complexes or free ions into the clay interlayer space by using post-synthesis intercalation procedures.[24,30] However, these synthetic protocols are quite expensive and require long preparation times. Moreover, depending on the complexes' stability, metal leaching processes can occur, thus leading to a potential environmental contamination and to toxic effects in different organisms. These disadvantages could be overcome by design synthetic strategies based on the direct insertion of the lanthanide ions in the clay synthesis gel, as previously performed with vanadium and niobium metals.[5,31,32]

Based on these considerations, in this study, two luminescent lanthanides, Tb^{3+} and Eu^{3+}, were simultaneously incorporated in the structure of a synthetic saponite clay (hereafter named Na-TbEuSAP), using a single-step hydrothermal approach. A solid with only Tb^{3+} ions was also prepared as a reference (hereafter named Na-TbSAP). A multi-technique characterization approach was employed to investigate the physico-chemical properties of the solids. These novel light-emitting saponites were also tested as potential optical sensors for inorganic anions in water. In this respect, it was proved that the lanthanide complexes, when incorporated in different hybrid solids or gels (*i.e.* metal–organic frameworks, polymers…), can be employed as efficient sensors for different kinds of substrates (ions and organic molecules) by exploiting the so-called "antenna effect" phenomena.[33,34] To the best of our knowledge, the lanthanide-based clays studied in the literature has never been investigated as sensors for the detection of anionic species.

Among the anions, the chromate (CrO_4^{2-}), a common source of the hexavalent chromium ($Cr^{(VI)}$) which is regarded as the most toxic and dangerous form of this element, was selected for the sensor tests.[35–38] The CrO_4^{2-} is an environmentally-hazardous inorganic pollutant commonly present in soils and waters, and it has been found in several public drinking waters worldwide as well near particular industrial plants.[35–38] The amount of chromium in water and soil is strictly regulated by international and national policies: *i.e.* the limit in drinking waters for EPA (United Sates Environmental Protection Agency) is of 100 ppb, while in Italy is even lower (50 ppb).[39,40] Thus, the development of efficient sensors for $Cr^{(VI)}$ compounds,

[a]*Dipartimento di Scienze e Innovazione Tecnologica, Università degli Studi del Piemonte Orientale "Amedeo Avogadro", Viale Teresa Michel 11, 15121-Alessandria, Italy. E-mail: fabio.carniato@uniupo.it*

[b]*CNR-SCITEC, Istituto di Scienze e Tecnologie Chimiche "G. Natta", Via C. Golgi 19, 20133-Milano, Italy*

† Electronic supplementary information (ESI) available. See DOI: 10.1039/d0ra05693f

especially in water media, is therefore of great importance in terms of public health and safety.

In detail, Na-TbEuSAP and Na-TbSAP samples were prepared by a modified one-pot hydrothermal synthesis protocol, followed by sodium-exchange process (Scheme S1 in the ESI†).[5,31,32] Eu^{3+} and Tb^{3+} were introduced in the form of chloride salts during the synthesis gel along with the silicon, aluminium and magnesium precursors. The final materials were then submitted to ionic exchange procedure to replace the different cations located in the saponite gallery (*i.e.* Al^{3+}, Mg^{2+}, H_3O^+) with Na^+ ions.

The lanthanides loading in the final materials was determined by inductively coupled plasma mass spectrometry (ICP-MS). The Tb^{3+} amount was found to be 0.021 and 0.031 mmol g^{-1} for TbSAP and TbEuSAP samples, respectively. For both solids, the Na^+-exchange procedure did not alter the amount of Tb^{3+} species. For TbEuSAP sample, the Eu^{3+} content resulted to be 0.023 mmol g^{-1}, without modification after the ion-exchange procedure. The differences in the Tb^{3+} concentrations observed in the two materials could be ascribed to a certain variability in the chemical composition of the samples, as testified by the different cationic exchange capacity of TbSAP and TbEuSAP (see below). In fact, numerous parameters (*i.e.* the acidity of the gel during the condensation phase, the amount of water, *etc*…) including the co-presence of two different metal ions in competition with similar structural sites can positively or negatively affect the final loading of the metal ions. In general, however, the results suggest that both metals are mainly located in the framework of the saponite clay, as schematically proposed in Fig. 1B.

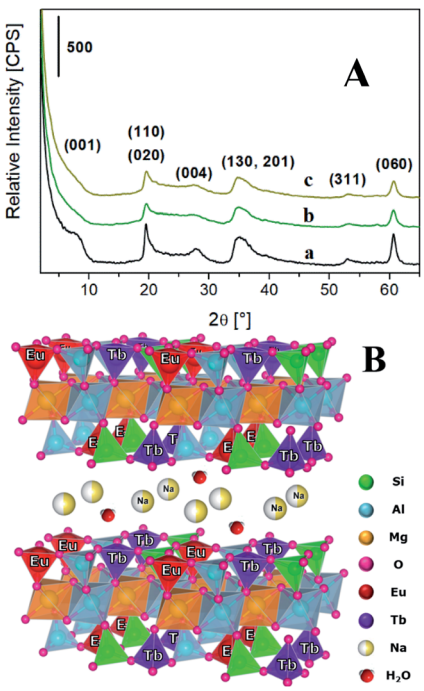

Fig. 1 (A) X-ray diffraction pattern of Na-SAP (a), Na-TbSAP (b) and Na-TbEuSAP (c) samples. (B) Schematic representation of the Na-TbEuSAP clay.

The inclusion of the lanthanides ions during the synthesis did not alter the layered structure of the saponite,[1–7,12,22,23] as indicated by the X-ray powder diffraction (XRPD) analyses (Fig. 1A). In particular, the X-ray patterns of Na-TbSAP and Na-TbEuSAP showed the typical reflections of the saponite clay. Nevertheless, the signal associated to the basal plane (001) in both samples, with *d*-spacing value in the 7.4–8.0° 2θ range, is less defined respect to the parent Na-SAP sample, thus indicating a greater structural disorder of the lamellae packing.[1]

The cation-exchange capacity (CEC) of the clays, evaluated by UV-Visible spectroscopy analysis[30,31] (Fig. S1 in the ESI†), was estimated to be 41.6 ± 4.8 meq./100 g and 61.2 ± 5.2 meq./100 g for Na-TbSAP and Na-TbEuSAP, respectively. These values are in line with the results obtained for other metal-containing saponites.[5,31,32]

The solids showed high thermal stability, as indicated by the thermogravimetric analyses (TGA). The TGA (Fig. S2A in the ESI†) and the derivative curves (DTG) (Fig. S2B in the ESI†) of Na-TbSAP (curve a) and Na-TbEuSAP (curve b) show a first weight loss around 100 °C related to the evaporation of physisorbed water, followed by a gradual release of the interlamellar water (with an initial dehydroxylation of the layered structure) in the 150–750 °C range. A third weight loss around 825 °C is correlated to the collapse of the saponite framework, with formation of the relative metal oxides.[1–4]

The photophysical properties of the luminescent saponites were thoroughly investigated by photoluminescence (PL) spectroscopy. The excitation spectra at solid state of Na-TbSAP and Na-TbEuSAP (Fig. 2A), collected at the most intense emission line of Tb^{3+} at 545 nm, showed a common broad band with a maximum at 270 nm associated to the $^7F_6$-5d electronic transition of Tb^{3+}.[41–43] Both spectra are also composed by another characteristic peak of Tb^{3+}, associated to its intra-$4f^8$ electronic transitions ($^7F_6$–^5D_J, $J = 2,3$).[41–43] When monitored at the most intense emission line of Eu^{3+} at 615 nm (Fig. 2Ac), the spectrum of Na-TbEuSAP presented the same bands, previously observed, along with additional peaks ascribed to the intra-$4f^6$ transitions of Eu^{3+} ($^7F_{0,1}$–^5H_J, ^5D_J, ^5L_J and ^5G_J), with a λ_{max} at 395 nm ($^7F_0$–$^5L_6$).[44–47] The presence of the Tb^{3+} transitions in the spectrum of Na-TbEuSAP analysed at the emission line of Eu^{3+} is a clear indication of the occurrence of a $Tb^{3+} \rightarrow Eu^{3+}$ metal-to-metal energy transfer (MMET) process.[48–51] This hypothesis was confirmed by analysing the emission spectra at the solid state of Na-TbEuSAP under irradiation at λ_{max} of Eu^{3+} (395 nm) and Tb^{3+} (270 nm) (Fig. 2B).

Indeed, the emission spectrum collected at 270 nm showed emission peaks of both Tb^{3+} ($^5D_4$–^7F_J, $J = 6$–3)[41–43] and Eu^{3+} ($^5D_0$–^7F_J, $J = 0$–4).[45–49] The $Tb^{3+} \rightarrow Eu^{3+}$ energy transfer photo-enhanced the luminescence of europium, as indicated by the increased intensity of the $^5D_0$–$^7F_2$ emission band of Eu^{3+} at 615 nm (compared to the same band obtained after direct excitation at 395 nm) of *ca.* 90%. This also suggests that Tb^{3+} and Eu^{3+} are probably located in close proximity, thus ensuring an efficient optical communication between them.[48–51]

Additional information on the local chemical environment surrounding the lanthanides were extrapolated from the collected emission spectra. An heterogeneous distribution of

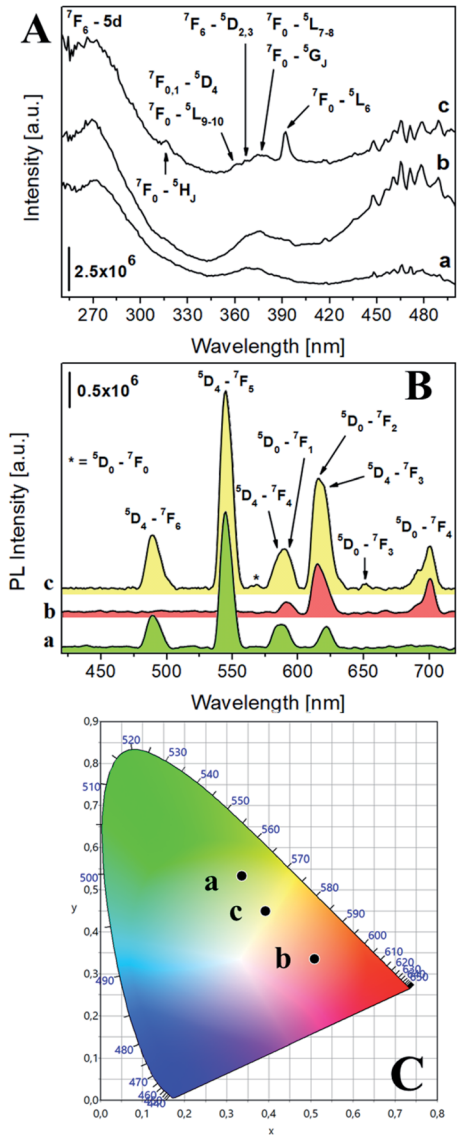

Fig. 2 (A) Excitation spectra at solid state of Na-TbSAP (a, $\lambda_{em} = 545$ nm) and Na-TbEuSAP (b, $\lambda_{em} = 545$ nm, c, $\lambda_{em} = 615$ nm). (B) Emission spectra at solid state of Na-TbSAP (a, $\lambda_{exc} = 270$ nm) and Na-TbEuSAP (b, $\lambda_{exc} = 395$ nm, c, $\lambda_{exc} = 270$ nm); the intensity of Na-TbSAP spectrum was normalized (divided by five) for a better comparison. (C) CIE 1931 *xy* chromaticity diagrams derived from emission spectra in frame B. The colour of each emission spectrum in frame B is associated to its corresponding *xy* coordinates (frame C and Table S2†).

the Eu^{3+} sites in the Na-TbEuSAP is derived by the presence of two weak peaks for the $^5D_0$–$^7F_0$ transition at *ca.* 560 nm (Fig. 2Bc).[52] The multiplicity of this band is commonly associated with the number of distinct chemical domains around the europium, since both its initial and final states are non-degenerated.[52] Moreover, the Eu^{3+} and Tb^{3+} centres in both clays are placed in a low symmetry environment, as suggested by the high values of their asymmetry factor ($R > 2$) (Table S1 in the ESI†). The *R* factor was calculated from the intensity ratio of electric-dipole/ED $^5D_0 \rightarrow {}^7F_2$ on magnetic-dipole/MD $^5D_0 \rightarrow {}^7F_1$ for Eu^{3+},[44–47,53,54] and of ED $^5D_4 \rightarrow {}^7F_5$/MD $^5D_4 \rightarrow {}^7F_6$ for Tb^{3+}.[55]

PL spectra allowed to extrapolate the colorimetric features of the samples, calculating their chromaticity coordinates (*xy*) and related parameters (RGB and Hex) according to CIE 1931 colour spaces (Fig. 2C and Table S2 in the ESI†).[56] A modulation of the colour emission was observed for the bi-functional saponite. Indeed, while the direct excitation of Eu^{3+} at 395 nm in Na-TbEuSAP led to an emission in the visible red region, the sample after excitation at 270 nm showed a blue shift towards a final yellow emission. As a comparison, the emission colour of Na-TbSAP is green.

The parameters that describe the Tb^{3+}–Eu^{3+} energy transfer process were derived by considering the experimental lifetimes of donor (D, Na-TbSAP) and donor–acceptor (DA, Na-TbEuSAP) systems, measured by time-resolved fluorescence spectroscopy.[48–51,57–59] The intensity decay curves of $^5D_4$ excited state of Tb^{3+} at $\lambda_{em} = 545$ nm ($^5D_4$–$^7F_6$) were collected at solid state, under excitation at 370 nm (Fig. S3 in the ESI†). The curves were fitted with a bi-exponential function, from which the average τ values were calculated. The energy transfer rate (k_{EnT}) and efficiency (E_{EnT}) parameters were calculated from eqn (1) and (2), using the lifetimes of the donor (Tb^{3+}) in the presence (τ_{DA}) or absence (τ_D) of the acceptor (Eu^{3+}), measured at 545 nm:[57–59]

$$K_{EnT}\left[s^{-1}\right] = \left(\frac{1}{\tau_{DA}} - \frac{1}{\tau_D}\right) \quad (1)$$

$$E_{EnT}(o\eta_{sens})[\%] = \left(1 - \frac{\tau_{DA}}{\tau_D}\right) \times 100 \quad (2)$$

The results, reported in Table 1, showed a high energy transfer efficiency of *ca.* 81%, with a rate constant of 74 100 s^{-1}. Surprisingly, the lifetime decay for Na-TbSAP is very low (5.66×10^{-5} s). A possible explanation is related to the fact that the first coordination sphere of the metal contains coordinated water molecules, adsorbed or intercalated in the solid material, which essentially determine the site lifetimes.

Finally, the luminescence at solid state of Na-TbSAP and Na-TbEuSAP proved to be stable even after 1 h of irradiation at 270 nm, as demonstrated in photobleaching tests reported in Fig. S4.†

Considering their interesting photophysical properties, the luminescent saponite samples were preliminarily tested for the optical detection of the chromate anion (CrO_4^{2-}) in water. For the sensing test, the samples were dispersed in water and then put in contact with different concentrations of CrO_4^{2-}, from 0.0001 to 1 mM. Subsequently, for each experimental point, an emission spectrum was collected. The PL spectra were obtained

Table 1 Experimental lifetimes (τ) of Na-TbSAP (D) and Na-TbEuSAP (DA), collected by monitoring the $^5D_4$–$^7F_5$ emission transition of Tb^{3+} at 545 nm under irradiation at 370 nm and the $Tb^{3+} \rightarrow Eu^{3+}$ energy transfer rate (k_{EnT}) and efficiency (E_{EnT})

τ_D [s]	τ_{DA} [s]	k_{EnT} [s^{-1}]	E_{EnT} [%]
5.66×10^{-5}	1.09×10^{-5}	7.41×10^4	80.74

at the two main λ_{exc} of Tb^{3+} and Eu^{3+} (270 and 395 nm, respectively), monitoring their emission bands at 545 and 615 nm (see in the ESI† for an accurate description of the procedure). The analyses were performed on the aqueous suspensions of Na-TbSAP and Na-TbEuSAP samples under continuous stirring, at room temperature. Prior the sensing tests, the suspensions stability of the saponites dispersed in water were carefully assessed by dynamic light scattering (DLS) analysis, performed at 25 °C (Fig. S5 in the ESI†). The suspensions remained qualitatively homogeneous and stable, with a hydrodynamic diameter of the particles of 16 and 35 nm (polydispersity index (PDI) of 0.71 and 0.65) for Na-TbSAP and Na-TbEuSAP, respectively. Nevertheless, the PDI index calculated for these samples must be carefully considered for two reasons: (i) the light emission properties of these samples can interfere with the laser source used for the analysis; (ii) the samples are composed by lamellae with different aspect ratio. Such particles morphology can influence the quality of the data analysis.

The emission spectra of the aqueous suspensions of Na-TbSAP and Na-TbEuSAP treated with progressive CrO_4^{2-} concentrations are reported in Fig. S6 in the ESI.† The suspensions of the samples analysed were stirred continuously at room temperature during the sensing tests, to maintain a good stability over time. First, the spectra collected before the addition of CrO_4^{2-} anions (black curves (a) in Fig. S6†) showed the typical emission peaks of Tb^{3+} and Eu^{3+},[41–47] as observed in the solid-state analyses reported in Fig. 2B. The spectra of pristine samples in water showed no intensity reduction over time, thus confirming the high suspensions stability in the experimental conditions adopted, without any effect of particles aggregation or deposition on the final optical properties.

Afterwards, the samples were put in contact with the CrO_4^{2-} anion. In the presence of increasing amount of CrO_4^{2-} (from red (b) to blue (c) curves in Fig. S6†), the intensity of the peaks at 545 and 615 nm decreased for both solids, thus suggesting that both metals are probably involved in the interaction with the anion.

The evolution of the normalized PL intensity of the band at 545 nm (λ_{exc} = 270 nm) as a function of the CrO_4^{2-} concentration is reported in Fig. 3A. For both Na-TbSAP and Na-TbEuSAP samples, an exponential decay of the intensity of the band at 545 nm is observed. In particular, a marked photoluminescence decrease after contacting the samples with a CrO_4^{2-} concentration of 1 μM (= 52 ppb of $Cr^{(VI)}$, lower than the EPA value of 100 ppb) is visible.[35–38] Indeed, the fluorescence is almost quenched for both samples with a CrO_4^{2-} concentration of 500 μM. In these experimental conditions, the Na-TbEuSAP displayed a PL intensity attenuation at 1 μM of 63% compared to the 15% of Na-TbSAP, implying a more rapid CrO_4^{2-} detection response which could be ascribed to differences in the chemical composition of the samples (*i.e.* loadings and localization of the metal sites,…).

Similar results have been obtained by monitoring the normalized PL intensity of the band at 615 nm of Na-TbEuSAP, under excitation at 270 nm and 395 nm (Fig. 3B). The peak intensity quickly decreases with a similar trend under both

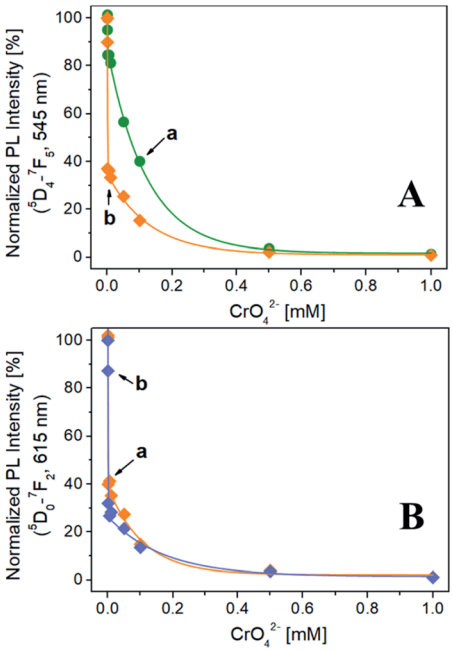

Fig. 3 (A) Normalized PL intensity of the band at 545 nm in the presence of different CrO_4^{2-} concentrations for Na-TbSAP (a) and Na-TbEuSAP (b). (B) Normalized PL intensity of the 615 nm band as a function of the different CrO_4^{2-} concentrations for Na-TbEuSAP at λ_{exc} = 270 (a) and 395 nm (b).

excitations. Under direct excitation at 395 nm, however, a slightly more rapid decline of the PL intensity was detected.

These preliminary tests demonstrated high sensing capabilities of Tb^{3+}/Eu^{3+}-saponite clays, with a rapid recognition of CrO_4^{2-} in water at low concentrations due to a marked quenching process, especially for Na-TbEuSAP sample. The sensing performance also proved to be highly modular: indeed, it is possible to easily monitor two distinct emission bands (545 and 615 nm) under two separate irradiations (270 and 395 nm).

The quenching mechanism is probably governed by diffusional phenomena of the CrO_4^{2-} anions between the clay particles. As commonly known, the saponite clays are very efficient cationic exchanger solids.[1] The diffusion of anions inside the interlayer space of clay is unlikely to happen. For these reasons, our hypothesis is that the interaction between the CrO_4^{2-} and the Tb^{3+}/Eu^{3+} sites may occur on the galleries entrance or on the particle's surfaces, between the clay tactoids, in accessible framework tetrahedral sites.[60] The interaction metal/substrate could also be favoured by the swelling of the saponite lamellae in water, which results in more exposed lanthanides centres to surrounding CrO_4^{2-} anions.[61]

The quenching efficiency was clarified in more detail with the aid of the Stern–Volmer relationship, which describes the kinetics of photophysical deactivation processes between a quencher molecule (Q) and an excited fluorophore (A*).[62–65] In our case, Q is the CrO_4^{2-} and A* is Eu^{3+} and Tb^{3+} ions. In general, two quenching processes are usually encountered: (1) static or SQE (formation of a Q–A 'complex' in the ground-state) and (2) dynamic or DQE (collisional). SQE and DQE are

governed by Stern–Volmer equations (eqn (S1) and (S2)), reported in the ESI.†[62–65] By plotting the evolution of F_0/F *vs.* $[Q]$, where F_0 and F are the fluorescence intensities of the 545 or 615 nm band without and in the presence of the quencher at different concentrations, it was possible to extrapolate the type of quenching process and calculate the relative quenching constants.[62–65] The Stern–Volmer plots reported in Fig. S7 in the ESI† exhibited an upward curvature in all the cases analysed, which is indicative of a quadratic relationship between fluorescence intensity and the anion concentrations, as reported in the literature.[63] This non-linear dependence, even at low concentrations, suggest that both static and dynamic quenching are occurring with the same fluorophore, in both clays. Similar behaviour was previously documented in the literature by Lin *et al.* to explain complex quenching mechanisms occurred for MnO_2 nanosheets towards Au nanocluster fluorescence.[63] The phenomenon is governed by a modified Stern–Volmer equation (eqn (S3) in the ESI†), from which ($K_D \times K_S$) and ($K_D + K_S$) parameters can be derived.[63] The combined quenching dynamic (K_D) and static (K_S) constants, obtained by fitting the data in Fig. S7† (Table S3 in the ESI†), indicate that the quenching efficiency is dependent on the excitation wavelength, the monitored emission signal and the presence of both lanthanides. In particular, the quenching seems to be more pronounced for Na-TbEuSAP.

The performance demonstrated for both samples in these preliminary tests are extremely encouraging, and are comparable to those of other luminescent probes based on MOFs mostly containing transitions metals and Eu^{3+},[66] Tb^{3+}-complexes,[67] coordinated polymers with Zn^{2+} and Tb^{3+},[68] and carbon quantum dots.[69]

Conclusions

In this study, for the first time two luminescent lanthanides ions (Tb^{3+} and Eu^{3+}) were successfully introduced in the framework of synthetic saponite clays through a simple one-pot hydrothermal method. The obtained samples, containing in the structure Tb^{3+} or a simultaneous combination of Tb^{3+} and Eu^{3+} ions, possessed good cation-exchange capacity, layered structure and high thermal stability. The luminescent clay showed interesting photoluminescence features. In particular, the co-presence of both metal centres in the framework gives rise to an efficient $Tb^{3+} \rightarrow Eu^{3+}$ energy transfer, that greatly enhances the europium luminescence. Moreover, the clay demonstrated a high stoke shift and tuneable emission colours. These excellent photophysical properties were exploited for the optical recognition of chromate anion in water, which is a common environmental pollutant and a source of hexavalent chromium. In the tests, all the luminescent solids demonstrated high photoluminescence sensing capabilities, directly exploiting the intrinsic optical properties of the two lanthanides, with a rapid detection response at very low concentrations (at μM level) due to a complex mixed static/dynamic quenching mechanism involved in the process.

The simple one-pot synthetic method and the attractive physico-chemical properties of these luminescent clays are extremely encouraging for the future development of new metal-containing clay materials with one or more functionalities. The materials prepared in this study could find application in the rational design of effective fluorescent sensors for targets of interest.

The use of photoluminescence spectroscopy for these purposes is expanding and has some important advantages respect to traditional elemental analyses techniques: (i) the sample does not require specific treatments before analysis, (ii) the measurement is fast and easy to perform, (iii) can be applied to different types of matrices. One of the main disadvantages is related to the poor selectivity for the identification of multiple species. This specific topic along with a more comprehensive overview of the sensing properties of the lanthanide-clays (*i.e.* detection limits and reusability) are currently under investigation.

Conflicts of interest

There are no conflicts to declare.

Acknowledgements

The authors are fully grateful to Mr Marco Barbetta for his help in the experiments and to Dr Elena Perin (DiSIT, Università del Piemonte Orientale, Alessandria, Italy) for ICP-MS analyses. Financial support from the Università del Piemonte Orientale (FAR-2019) is also acknowledged.

Notes and references

1 (*a*) F. Carniato, G. Gatti and C. Bisio, *New J. Chem.*, 2020, **44**, 9969–9980; (*b*) G. Paul, C. Bisio, I. Braschi, M. Cossi, G. Gatti, E. Gianotti and L. Marchese, *Chem. Soc. Rev.*, 2018, **47**, 5684–5739.

2 D. Costenaro, G. Gatti, F. Carniato, G. Paul, C. Bisio and L. Marchese, *Microporous Mesoporous Mater.*, 2012, **162**, 159–167.

3 C. Bisio, G. Gatti, E. Boccaleri, G. Superti, H. Pastore and M. Thommes, *Microporous Mesoporous Mater.*, 2008, **107**, 90–101.

4 (*a*) C. Bisio, G. Gatti, E. Boccaleri, L. Marchese, L. Bertinetti and S. Coluccia, *Langmuir*, 2008, **24**, 2808–2819; (*b*) C. Bisio, F. Carniato, G. Paul, G. Gatti, E. Boccaleri and L. Marchese, *Langmuir*, 2011, **27**, 7250–7257.

5 F. Carniato, C. Bisio, R. Psaro, L. Marchese and M. Guidotti, *Angew. Chem., Int. Ed.*, 2014, **53**, 10095–10098.

6 F. Carniato, C. Bisio, G. Gatti, E. Boccaleri, L. Bertinetti, S. Coluccia, O. Monticelli and L. Marchese, *Angew. Chem., Int. Ed.*, 2009, **48**, 6059–6061.

7 M. Guidotti, R. Psaro, N. Ravasio, M. Sgobba, F. Carniato, C. Bisio, G. Gatti and L. Marchese, *Green Chem.*, 2009, **11**, 1173–1178.

8 G. Mata, R. Trujillano, M. A. Vicente, C. Belver, M. Fernández-García, S. A. Korili and A. Gil, *Appl. Catal., A*, 2007, **327**, 1–12.

9 L. A. Utracki, M. Sepehr and E. Boccaleri, *Polym. Adv. Technol.*, 2007, **18**, 1–37.
10 M. Mokhtar, *Materials*, 2017, **10**, 760–772.
11 M. I. Boyanov, D. E. Latta, M. M. Scherer, E. J. O'Loughlin and K. M. Kemner, *Chem. Geol.*, 2017, **464**, 110–117.
12 S. Marchesi, F. Carniato, M. Guidotti, M. Botta, L. Marchese and C. Bisio, *New J. Chem.*, 2020, **44**, 10033–10041.
13 Y.-C. Lee, T.-H. Lee, H.-K. Han, W. J. Go, J.-W. Yang and H.-J. Shin, *Photochem. Photobiol.*, 2010, **86**, 520–527.
14 F. Olivero, F. Carniato, C. Bisio and L. Marchese, *J. Mater. Chem.*, 2012, **22**, 25254–25261.
15 X. Chen, Y. Xu, H. Li and B. Liu, *Sens. Actuators, B*, 2017, **246**, 344–351.
16 (*a*) J. Rocha, L. D. Carlos, F. A. A. Paz and D. Ananias, *Chem. Soc. Rev.*, 2011, **40**, 926–940; (*b*) J. Rocha and L. D. Carlos, *Curr. Opin. Solid State Mater. Sci.*, 2003, **7**, 199–205.
17 (*a*) J. Rocha, L. D. Carlos, A. Ferreira, J. P. Rainho, D. Ananias and Z. Lin, *Mater. Sci. Forum*, 2004, **455–456**, 527–531; (*b*) D. Ananias, A. Ferreira, J. Rocha, P. Ferreira, J. P. Rainho, C. Morais and L. D. Carlos, *J. Am. Chem. Soc.*, 2011, **123**, 5735–5742.
18 (*a*) V. Balzani, P. Ceroni and A. Juris, *Photochemistry and Photophysics: Concepts, Research, Applications*, 2014, Wiley-VCH Verlag GmbH & Co, Weinheim, ISBN: 978-3-527-33479-7; (*b*) J.-C. G. Bünzli, *Coord. Chem. Rev.*, 2015, **293–294**, 19–47.
19 (*a*) A. F. Mingo, S. C. Serra, S. Baroni, C. Cabella, R. Napolitano, I. Hawala, I. M. Carnovale, L. Lattuada, F. Tedoldi and S. Aime, *Magn. Reson. Med.*, 2016, **78**, 1523–1532; (*b*) D. Parker, *Handbook on the Physics and Chemistry of Rare Earths*, ed. J.-C. G. Bünzli and V. K. Pecharsky, Elsevier, Amsterdam, 2016, vol. 50, pp. 269–299, ISBN: 978-0-444-63851-9.
20 F. Carniato, L. Tei and M. Botta, *Eur. J. Inorg. Chem.*, 2018, 4936–4954.
21 (*a*) D. Ananias, F. A. A. Paz, L. D. Carlos and J. Rocha, *Chem.–Eur. J.*, 2018, **24**, 11926–11935; (*b*) J. Rocha, C. D. S. Brites and L. D. Carlos, *Chem.–Eur. J.*, 2016, **22**, 14782–14795.
22 S. L. C. Pinho, H. Faneca, C. F. G. C. Geraldes, J. Rocha, L. D. Carlos and M.-H. Delville, *Eur. J. Inorg. Chem.*, 2012, 2828–2837.
23 M. Jin, D. E. M. Spillane, C. F. G. C. Geraldes, G. R. Williams and S. W. A. Bligh, *Dalton Trans.*, 2015, **44**, 20728–20734.
24 (*a*) S. Marchesi, F. Carniato, C. Bisio, L. Tei, L. Marchese and M. Botta, *Dalton Trans.*, 2018, **47**, 7896–7904; (*b*) D. Lalli, S. Marchesi, F. Carniato, C. Bisio, L. Tei, L. Marchese and M. Botta, *Dalton Trans.*, 2020, **49**, 6566–6571.
25 (*a*) D. Talarico de Araujo, K. J. Ciuffi, E. J. Nassar, M. A. Vicente, R. Trujillano, P. S. Calefi, V. Rives and E. H. de Faria, *J. Phys. Chem. C*, 2017, **121**, 5081–5088; (*b*) H. Li, M. Li, Y. Wang and W. Zhang, *Chem.–Eur. J.*, 2014, **20**, 10392–10396.
26 (*a*) Y. Wang, P. Li, S. Wang and H. Li, *J. Rare Earths*, 2019, **37**, 451–467; (*b*) S.-J. Ruy, A. Kim, M. D. Kim, S. W. Hong, S. S. Min, J.-H. Lee, J.-K. Lee and H. Jung, *Appl. Clay Sci.*, 2014, **101**, 52–59.
27 X. Chen, Y. Wang, R. Chai, Y. Xu, H. Li and B. Liu, *ACS Appl. Mater. Interfaces*, 2017, **9**, 13554–13563.
28 D. Yang, Y. Wang, Y. Wang and H. Li, *Sens. Actuators, B*, 2016, **235**, 206–212.
29 J. A. Peters and K. Djanashvili, *Eur. J. Inorg. Chem.*, 2012, 1961–1974.
30 E. M. Kovacs, E. E. Baradacs, P. Konya, P. Kovacs-Palffy, S. Harangy, E. Kuzmann, J. Konya and N. M. Nagy, *Colloids Surf., A*, 2017, **522**, 287–294.
31 L. Ostinelli, S. Recchia, C. Bisio, F. Carniato, M. Guidotti, L. Marchese and R. Psaro, *Chem.–Asian J.*, 2012, **7**, 2394–2402.
32 D. Costenaro, C. Bisio, F. Carniato, S. L. Safronyuk, T. V. Kramar, M. V. Taran, M. F. Starodub, A. M. Katsev and M. Guidotti, *ChemistrySelect*, 2017, **2**, 1812–1819.
33 (*a*) F. Liu, W. Gao, P. Li, X.-M. Zhang and J.-P. Liu, *J. Solid State Chem.*, 2017, **253**, 202–210; (*b*) Z. Zhou, Q. Wang and C. Tan, *Soft Mater.*, 2014, **12**, 98–102.
34 (*a*) P. D. Beer and P. A. Gale, *Angew. Chem., Int. Ed.*, 2001, **40**, 486; (*b*) C. Suksai and T. Tuntulani, *Chem. Soc. Rev.*, 2003, **32**, 192.
35 (*a*) H. Sun, J. Brocato and M. Costa, *Curr. Environ. Health Rep.*, 2015, **2**, 295–303; (*b*) H. Oliveira, *J. Bot.*, 2012, 1–8.
36 (*a*) NASA Principal Center for Regulatory Risk Analyses and Communication, *Regulatory Considerations for Chromium*, http://www.rracps.org, retrieved on May 2020; (*b*) IARC (International Agency for Research on Cancer), *Volume 100C: Arsenic, Metals, Fibres, and Dusts*, 2012, Lyon, ISBN: 978-92-832-0135-9.
37 S. Mishra and R. N. Bharagava, *J. Environ. Sci. Health, Part C: Environ. Carcinog. Ecotoxicol. Rev.*, 2015, **34**, 1–32.
38 A. K. Shanker, C. Cervantes, H. Loza-Tavera and S. Avudainayagam, *Environ. Int.*, 2005, **31**, 739–753.
39 (*a*) https://www.culligan.it/cromo-nelle-acque/, retrieved on , May 2020; (*b*) Ministero della Salute (Italia), *Direzione Generale della Prevenzione Sanitaria, Scheda "Acque Potabili – Parametri, Cromo"*, 2016, http://www.salute.gov.it/portale/temi/documenti/acquepotabili/parametri/scheda_CROMO.pdf, retrieved on May 2020; (*c*) https://www.epa.gov/sdwa/chromium-drinking-water, retrieved on , May 2020.
40 R. Bevan, *Word Health Organization (WHO) Guidelines for Drinking-water Quality, Chromium in Drinking-water*, 2019, retrieved on May 2020.
41 S. Cotton, *Lanthanide and Actinide Chemistry*, 2016, John Wiley & Sons, Inc., ISBN: 978-0-470-01005-1.
42 Q. Li, T. Li and J. Wu, *J. Phys. Chem. B*, 2001, **105**, 12293–12296.
43 A. Podhorodecki, N. V. Gaponenkop, M. Banski, T. Kim and J. Misiewicz, *ECS Trans.*, 2010, **28**, 81–88.
44 Y. Wang and N. Lin, *Photochem. Photobiol. Sci.*, 2011, **10**, 42–47.
45 S. Marchesi, F. Carniato and E. Boccaleri, *New J. Chem.*, 2014, **38**, 2480–2485.
46 S. Marchesi, F. Carniato and E. Boccaleri, *ChemPlusChem*, 2015, **80**, 915–918.

47 S. Marchesi, C. Bisio, E. Boccaleri and F. Carniato, *ChemPlusChem*, 2020, **85**, 176–182.
48 (*a*) D. T. de Lill, A. de Bettencourt-Dias and C. L. Cahill, *Inorg. Chem.*, 2007, **46**, 3960–3965; (*b*) A. M. Kaczmarek and P. Van Der Voort, *Materials*, 2020, **13**, 566–593.
49 M. O. Rodrigues, J. D. L. Dutra, L. A. O. Nunes, G. F. de Sá, W. M. de Azevedo, P. Silva, F. A. A. Paz, R. O. Freire and S. A. Junior, *J. Phys. Chem. C*, 2012, **116**, 19951–19957.
50 X. Zhou, L. Chen, Z. Feng, S. Jiang, Y. Pang, L. Li and G. Xiang, *Inorg. Chim. Acta*, 2018, **469**, 576–5820.
51 X.-Y. Li, W.-J. Shi, X.-Q. Wang, L.-N. Ma, L. Hou and Y.-Y. Wang, *Cryst. Growth Des.*, 2017, **17**, 4217–4224.
52 K. Binnemans and C. Gorller-Walrand, *J. Rare Earths*, 1996, **14**, 173–180.
53 S. F. Tang, A. Babai and A. V. Mudring, *Angew. Chem., Int. Ed.*, 2008, **47**, 7631–7638.
54 P. Zhang, Y. Wang, H. Liu and Y. Chen, *J. Mater. Chem.*, 2011, **21**, 18462–18466.
55 H. Yin, Y. Li, J. Bai, M. Ma and J. Liu, *J. Materiomics*, 2017, **3**, 144–149.
56 I. P. Sahu, D. P. Bisen, R. K. Tamrakar, K. V. R. Murthy and M. Mohapatra, *Journal of Science: Advanced Materials and Devices*, 2017, **2**, 59–68.
57 (*a*) A. Katiyar, S. Yadav, P. G. Smirniotis and N. G. Pinto, *J. Chromatogr. A*, 2006, **1122**, 13; (*b*) M. Kruk, M. Jaroniec, Y. Sakamoto, O. Terasa-ki, C. H. Ko and R. Ryoo, *J. Phys. Chem. B*, 2000, **104**, 292.
58 K. Binnemans, *Coord. Chem. Rev.*, 2015, **295**, 1–45.
59 (*a*) F. Olivero, F. Carniato, C. Bisio and L. Marchese, *Chem.–Asian J.*, 2013, **9**, 158–165; (*b*) F. Cucinotta, F. Carniato, A. Devaux, L. De Cola and L. Marchese, *Chem.–Eur. J.*, 2012, **18**, 15310–15315.
60 (*a*) R. A. Schoonheydt and C. T. Johnston, The surface properties of clay minerals, *Layered Mineral Structures and their Application in Advanced Technologies*, M. F. Brigatti and A. Mottana, 2011; (*b*) A. Doi, M. Ejtemaei and A. V. Nguyen, *Miner. Eng.*, 2019, **143**, 105929.
61 (*a*) K. Norrish, *Nature*, 1954, **1**, 120–134; (*b*) M. L. Whittaker, L. N. Lammers, S. Carrero, B. Gilbert and J. F. Banfield, *PNAS*, 2019, **116**, 22052–22057; (*c*) M. A. Chapperl, D. A. Laird, M. L. Thompson, H. Li, B. J. Teppen, V. Aggarwal, C. T. Johnston and S. A. Boyd, *Environ. Sci. Technol.*, 2005, **39**, 3150–3156; (*d*) H. Suquet, C. de la Calle and H. Pezerat, *Clays Clay Miner.*, 1975, **23**, 1–9.
62 E. Blatt, R. C. Chatelier and W. H. Sawyer, *Biophys. J.*, 1986, **50**, 349–356.
63 S. Lin, H. Cheng, Q. Ouyang and H. Wei, *Anal. Methods*, 2016, **8**, 3935–3940.
64 M. H. Gehlen, *J. Photochem. Photobiol., C*, 2020, **42**, 100338.
65 M. A. Omary and H. H. Patterson, *Encyclopedia of Spectroscopy and Spectrometry, Luminescence Theory*, 2017, Elsevier Ltd., pp. 636–653.
66 (*a*) X. Zhuang, N. Zhang, X. Zhang, Y. Wang, L. Zhao and Q. Yang, *Microchem. J.*, 2019, 104498; (*b*) S. Mukherjee, S. Ganguly, D. Samanta and D. Das, *ACS Sustainable Chem. Eng.*, 2020, **8**, 1195–1206; (*c*) T. Kundu, K. Manna, A. K. Jana and A. Natarajan, *New J. Chem.*, 2019, **43**, 13263–13270; (*d*) W. Liu, Y. Wang, Z. Bai, Y. Li, Y. Wang, L. Chen, L. Xi, J. Diwu, Z. Chai and S. Wang, *ACS Appl. Mater. Interfaces*, 2017, **9**, 16448–16457; (*e*) A. K. Jana and S. Natarajan, *ChemPlusChem*, 2017, **82**, 1153–1163.
67 W. Yang, J. Xia, G. Zhou, T. Hu, D. Ye, D. Jiang and Q. Li, *Bull. Korean Chem. Soc.*, 2019, DOI: 10.1002/bkcs.11495.
68 (*a*) X. Feng, R. Li, L. Wang, S. W. Ng, G. Qin and L. Ma, *CrystEngComm*, 2015, **17**, 7878–7887; (*b*) T.-Y. Gu, M. Dai, D. J. Young, Z.-G. Ren and J.-P. Lang, *Inorg. Chem.*, 2017, **56**, 4668–4678.
69 (*a*) Y. Liu, Z. Chen, W. Li, C. Ma, P. Wu, X. Wu, S. Li and S. Liu, *Microchim. Acta*, 2018, **185**; (*b*) R. Vaz, J. Bettini, J. G. F. Júnior, E. D. S. Lima, W. G. Botero, J. C. C. Santos and M. A. Schiavon, *J. Photochem. Photobiol., A*, 2017, **346**, 502–511.